Energy Conversion and Management: X 23 (2024) 100651

Contents lists available at ScienceDirect

Energy Conversion and Management: X

journal homepage: www.sciencedirect.com/journal/energy-conversion-and-management-x

Exploring kinetics and mass transfer in photocatalytic CO_2 reduction: Impact of photocatalyst loading and stirrer speed

María de los Milagros Ballari [a,*], Miroslava Filip Edelmannová [b], Rudolf Ricka [b], Martin Reli [b], Kamila Kočí [b]

[a] Instituto de Desarrollo Tecnológico para la Industria Química (Universidad Nacional del Litoral - Consejo Nacional de Investigaciones Científicas y Técnicas), Ruta Nacional N° 168, 3000 Santa Fe, Argentina
[b] Institute of Environmental Technology, CEET, VŠB-Technical University of Ostrava, 17. Listopadu 15/2172, Ostrava-Poruba 70800, Czech Republic

ARTICLE INFO

Keywords:
Photocatalysis
Titanium dioxide
CO_2 reduction
Water splitting
Mathematical modelling
Mass transfer
Kinetic study

ABSTRACT

CO_2 photocatalytic reduction is a potential and promising technology to reduce the level of the greenhouse gas in the atmosphere but also as an alternative and renewable fuel resource. However, the products yield of the reaction is still low and the identification of the optimal operating conditions that affect the process are still needed to be determined. This study investigates the impact of key operational parameters, specifically photocatalyst concentration and stirring speed, on the photocatalytic reduction of CO_2 in a slurry batch photoreactor utilizing synthesized TiO_2. A simplified photocatalytic kinetic model, incorporating the radiation field within the photoreactor, was developed, considering mass transfer from liquid to gas phase for the primary detected reaction products (CO, CH_4, and H_2). The proposed models elucidate the influence of different operating conditions on product yields. Stirring speed, controlled by a magnetic stirrer, impacts the gas–liquid mass transfer rate. Increased liquid phase stirring speed ensures faster species transport to the gas phase, with a diminishing effect beyond 900 rpm. TiO_2 photocatalyst mass concentration influences the available total active surface and irradiation absorbance in the photoreactor volume. Optimal product yields were observed at the lowest tested photocatalyst concentration (0.5 $g \cdot L^{-1}$), indicating improved irradiation distribution and reduced particle agglomeration, resulting in higher available active surface for the reaction. The calculation model successfully predicted product yields even with lower photocatalyst concentration of 0.25 $g \cdot L^{-1}$, with marginal increases in predicted yields. These findings provide valuable insights for scaling up and optimizing the CO_2 photocatalytic reduction process, offering a foundation for future research.

1. Introduction

One of the most addressed problems of nowadays is energy production from non-renewable fossil fuels. Not only the fossil fuels are beginning to be scarce but their combustion produces, among others, carbon dioxide, a primary greenhouse gas, with approximately 31.5 billion tons generated worldwide per year from fossil fuels combustion [1]. So, photocatalytic reduction of carbon dioxide seems to be a promising way how to address these both society problems [2–8].

During last decades, many attempts were used for lowering the CO_2 emissions, like CO_2 capture, storage and utilization [9–12]. However, storage overcomes the problem only temporarily. Therefore, transforming CO_2 into useful compounds is necessary in order to solve the CO_2 problem permanently. Unfortunately, the methods mentioned above require high energy input, either high temperature and/or high pressure. Compared to these strategies, the photocatalytic reduction of CO_2 does not require any energy input other than solar radiation. Based on this fact, it can be considered one of the most attractive pathways for successfully converting CO_2 molecules into valuable compounds such as hydrocarbons (for example, methane). Moreover, the successful application of this technology can potentially lead to a long-term solution to reduce CO_2 emissions, thereby contributing to solving the issues of global warming and the energy crisis [13,14].

Unfortunately, the photocatalytic conversion of carbon dioxide is still very low. This reaction is a very complicated combination of photophysical and photochemical processes. Formation of the desired products – methane or methanol – is more difficult than the formation of other possible products like carbon monoxide, formaldehyde and formic acid. The reason lies in the kinetic drawback as the former

* Corresponding author.
E-mail addresses: ballari@santafe-conicet.gov.ar (M.M. Ballari), kamila.koci@vsb.cz (K. Kočí).

https://doi.org/10.1016/j.ecmx.2024.100651
Received 2 May 2024; Received in revised form 15 June 2024; Accepted 17 June 2024
Available online 20 June 2024

Nomenclature

A_R	(cm^2) area of the reactor window
A^{G-L}	(cm^2) area of the gas–liquid interface
a_V^{G-L}	(cm^{-1}) gas–liquid interfacial area per total volume of the reactor
A^{TiO_2}	(cm^2) total area of TiO_2
$a_V^{TiO_2}$	(cm^{-1}) active catalytic surface per liquid phase volume
b	(−) mass transfer exponent
$C_{G,i}$	($mol \cdot cm^{-3}$) products concentration in the gas phase
$C_{L,i}$	($mol \cdot cm^{-3}$) products concentration in liquid phase
$C_{L,i}^{int}$	($mol \cdot cm^{-3}$) gas – liquid equilibrium product concentration in liquid phase
C_{mc}	($g \cdot cm^{-3}$) photocatalyst load
D_R	(cm) reactor diameter
D_{iB}	($cm \cdot s^{-1}$) Diffusion coefficient of component i in B
$\langle e_\lambda^a \rangle_{V_L}$	($mW \cdot cm^{-3}$) Average Local Volumetric Rate of Photons Absorption in liquid phase
H	(−) Henrýs law constant
H_R	(cm) reactor height
I	($mW \cdot cm^{-2}$) light intensity
$< I >_{V_L}$	($mW \cdot cm^{-2}$) average radiation intensity in the liquid phase volume
k_{G-L}	($cm \cdot h^{-1}$) overall gas–liquid mass transfer coefficient
k'	(−) mass transfer parameter
L	(cm) length of the spectrometer cell
n	(−) light intensity reaction order
N	(rpm) stirring speed
R	(−) reflectance
$r_{G-L,\,i}$	($mol \cdot cm^{-2} \cdot h^{-1}$) interfacial mass transfer rate of product
r_i	($mol \cdot cm^{-2} \cdot h^{-1}$) local superficial product generation rate
$< r_i >_{V_L}$	($mol \cdot cm^{-2} \cdot h^{-1}$) average superficial reaction rate in the liquid phase volume
Re	(−) Reynolds number
S_g	($cm^2 \cdot g^{-1}$) specific surface of the photocatalyst
Sc	(−) Schmidt number
Sh	(−) Sherwood number
t	(h) time
T	(−) transmittance
V_R	(mL) reactor volume
V_L	(mL) liquid phase volume
V_G	(mL) gas phase volume
z	(cm) longitudinal coordinate

Greek letters

α_i	($mol \cdot cm^{2n-2} \cdot h^{-1} \cdot mW^{-n}$) reaction constant
β*	($L \cdot g^{-1} \cdot cm^{-1}$) specific extinction coefficient
ε	(−) liquid phase volume to reactor volume ratio ($=V_L/V_R$)
κ*	($L \cdot g^{-1} \cdot cm^{-1}$) specific absorption coefficient
λ	(nm) wavelength
μ	($kg \cdot m^{-1} \cdot s^{-1}$) viscosity
ρ	($g \cdot cm^{-3}$) density
σ*	($L \cdot g^{-1} \cdot cm^{-1}$) specific scattering coefficient

Special symbols

$\langle\ \rangle$	average

reactions require more electrons. In addition, the water splitting and CO_2 reduction reactions compete for the electrons in a reductive media producing hydrogen [15]. However, this by-product represents another a promising candidate for replacing fossil fuels without adversely affecting the environment. In addition, at the surface of the photocatalyst the holes may react with adsorbed water or hydroxide ions to generate hydroxyl radicals which can not only oxidize some intermediate products halting the process but also act as the adsorption sites for water, thereby reducing the adsorption of CO_2 molecules [16–18].

In photocatalytic applications, CO_2 conversion and yield rates could only be enhanced if equal importance is given to both efficient photocatalysts and optimal design of the photoreactors. While significant progress has been made in developing innovative materials for photocatalytic reduction reactions [19–23], the design, analysis, and optimization of photoreactors still demand further investigation. Various configurations of photoreactors have been employed for CO_2 photocatalytic reduction, including systems with suspended photocatalysts or immobilized photocatalysts, and reactors operating in three phases (gas–liquid-solid) or two phases (gas–solid) [24]. Among the fixed-bed reactors used for CO_2 photocatalytic reduction, the monolith and annular reactors are the most common [25]. However, slurry photoreactors, where the photocatalyst is suspended in a liquid phase, remain one of the simplest and most widely used configurations for studying the CO_2 reduction kinetics and performance of new photocatalytic materials. This is due to their high surface area-to-volume ratio, straightforward construction, and ease of design [24].

The kinetics of CO_2 photocatalytic reduction and the products formation over different kinds of photocatalysts have been the object of several studies. This fact is substantiated by the works of, for example, Kočí et al. [26], Tan et al. [27], Maarisetty et al. [5], and Thompson et al. [28], who investigated the photocatalytic CO_2 reduction kinetics with TiO_2 photocatalysts, while Bafaqeer et al. [29] explored the kinetics of the process utilizing g–C_3N_4–based composite photocatalysts. In particular, the majority of them suggest the application of a Langmuir – Hinshelwood type expressions. However, major enforces regarding theoretical analysis are required to comprehend and enhance the performance of this kind of reductive photocatalytic systems.

In this work, theoretical models are proposed to understand the photocatalytic CO_2 reduction, which can be useful for the reactor optimization to carry out the process. Based on the photocatalytic mechanism, simplified kinetic expressions were developed including the radiation field distribution in the photoreactor. The mass transfer of the main detected products – CO, CH_4 and H_2 – from the TiO_2 suspension to gas phase was considered to perform the mass balance of the slurry photoreactor. The main tested operating conditions were the stirring speed of batch photoreactor and the photocatalyst mass concentration.

2. Experimental

2.1. Photocatalyst preparation and characterization

TiO_2 anatase was prepared by a preparation approach, combining utilization of titanyl sulphate as a precursor and pressurized water processing [30]. Pressurized water processing was done for precursors made by induced hydrolysis method. The 0.16 mm $TiO(OH)_2$ size fraction was crystallized to TiO_2 with subcritical water in a flow-through mode at 200 °C and 10 MPa using 1.05 L H_2O (Section S1 and Fig. S1 of the Supplementary Information).

A detailed description of the experimental apparatus and the characterization techniques used, namely X-ray powder diffraction (XRD) and UV–Vis spectroscopy is provided in the Supplementary Information (Section S2).

2.2. Photocatalytic tests

The photocatalytic reduction of carbon dioxide was carried out in a homemade apparatus (Fig. 1). The main dimensions, characteristics and operating conditions are shown in Table 1.

A stirred batch cylindrical photoreactor (stainless steel, 356.5 mL) with the suspended photocatalyst was illuminated by a pen-ray 8 W Hg lamp with a peak light intensity at 254 nm (Ultra-Violet Products Inc., USA, 11SC-1) situated on the quartz glass window at the top of the photoreactor. The spectral emission of the lamp was determined by a fiber optic spectrometer (Ocean Optics USB 2000 + UV–Vis-ES) and it is shown in Fig. S2 of the Supplementary Information. The photocatalyst powder (0.06, 0.12 and 0.18 g TiO_2) was suspended in 120 mL of 0.2 M NaOH solutions for typical batches. A magnetic stirrer at the bottom agitated the catalyst-suspended solution to prevent sedimentation of the catalyst. The pressure of the gas phase was continuously monitored. Radiation intensity at different position at the liquid – gas interface was obtained by UVC light meter (Extech instruments SDL470) in a darkened laboratory (Fig. S3 of the Supplementary Information).

Prior to the illumination, CO_2 was bubbled with a constant flow through the stirred suspension for at least 25 min to purge the air and to saturate the solution. The pH of NaOH solution was measured before to start CO_2 saturation (pH = 12.4) and after the CO_2 saturation (pH = 6.7). According to the measurements performed with a Total Organic Carbon (TOC) analyzer (FormacsTM HT-I, Skalar Analytical B.V., Netherlands), the Dissolved Inorganic Carbon (DIC) at the end of the saturation with CO_2 was 0.25 mol · L^{-1}. The reactor was tightly closed and the CO_2 pressure was maintained at 120 kPa. Then the photocatalytic reaction was started by switching on the Hg lamp.

Samples of gas phase were taken at various times during the irradiation using a gas-tight syringe (10 mL) through a septum and the samples were immediately analyzed.

Blank reactions were performed to ensure that the hydrocarbon production was due to the photoreduction of CO_2 and to eliminate the surrounding interference. The first blank was UV-illuminated without the photocatalyst and the second was in the dark with the photocatalyst and CO_2 under the same experimental conditions. No hydrocarbons were detected in the above blank tests.

The first part of the measurements was carried out at different speeds of the agitator. Stirrer speed was 300, 500 and 700 rpm. The amount of photocatalyst was 0.12 g.

The second part of measurements, with the stirrer speed of 700 rpm was carried out changing the amount of catalyst. The amount of catalyst was 0.06 g, 0.12 g and 0.18 g.

All measurements were performed at least three times with a small variation in yield (less than 5 %). Each time the same batch was used but again bubbled with CO_2 and then irradiation was started. No photocatalyst deactivation was detected after subsequence cycles of reaction.

Table 1
Main dimension, characteristic and operating conditions of the experimental setup.

Parameter	Value	Units
Reactor height, H_R	7.8	cm
Reactor diameter, D_R	7.6	cm
Total reactor volume, V_R	356.5	mL
Liquid phase volume, V_L	120	mL
Gas phase volume, V_G	236.5	mL
UV-C Hg lamp power	8	W
Emission lamp wavelength, λ	254	nm
Lamp length	4.4	cm
Stirring speed, N	300–700	rpm
Catalyst mass concentration, C_{mc}	0.5–1.5	g · L^{-1}
CO_2 pressure	120	kPa
NaOH concentration	0.2	mol · L^{-1}

The gas phase samples were analyzed using a gas chromatograph (Shimadzu Tracera GC-2010Plus, JP) equipped with a barrier discharge ionization detector (BID) which is utilizing helium plasma and is very sensitive toward all monitored products (detection limits < 1 ppm). Used column in GC was ShinCarbon ST 80/100. The main products followed during the reactions were H_2, CO and CH_4. The calibration with certified calibration gases was performed before each experimental run.

3. Theoretical models

3.1. Extinction and absorption coefficients

The specific radiation extinction coefficient can be determined through a linear regression employing the experimental specular transmittance at 254 nm (Fig. S4 a) of the Supplementary Information) [31]. The following solution for the light intensity balance in the spectrophotometer cell can be applied:

$$-\ln\frac{I_\lambda}{I_{\lambda,0}} = -\ln\ T_{\lambda,S} = \beta^*_\lambda C_{mc} L \tag{1}$$

Where $T_{\lambda,S}$ is the specular transmittance at λ wavelength, C_{mc} is the catalyst mass concentration, L is the length of the spectrophotometer cell (1 cm), and β^*_λ is the specific extinction coefficient, being the sum of the absorption coefficient (κ^*_λ) and the scattering coefficient (σ^*_λ):

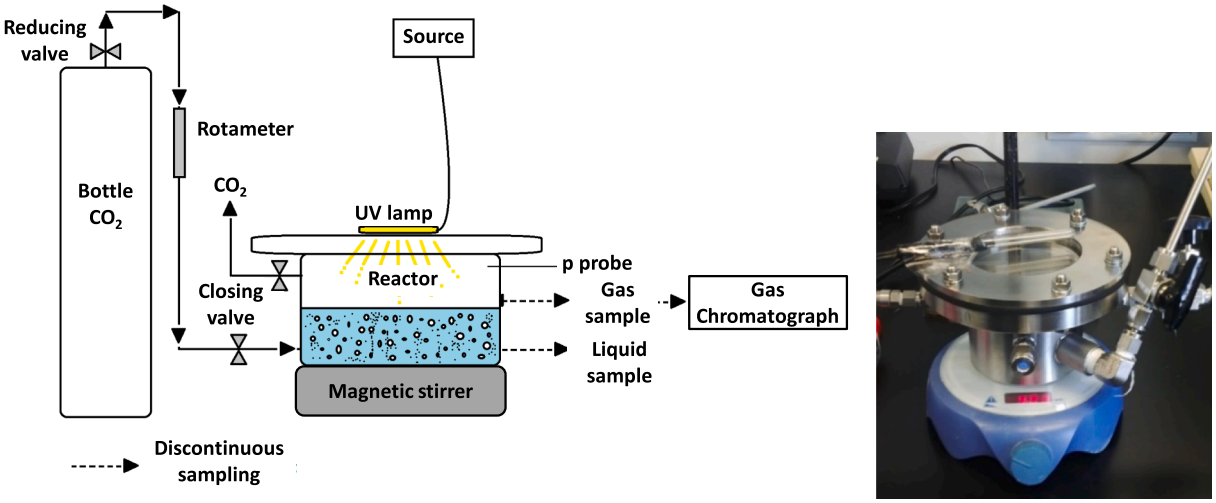

Fig. 1. Experimental setup for the CO_2 photocatalytic reduction.

$$\beta_\lambda^* = \kappa_\lambda^* + \sigma_\lambda^* \tag{2}$$

To calculate the absorption coefficient, an approximation is the application of the following equation using the experimental diffuse transmittance of the TiO_2 suspension:

$$-\ln\frac{I_\lambda}{I_{\lambda,0}} = -\ln\ T_{\lambda,D} = \kappa_\lambda^* C_{mc} L \tag{3}$$

Where T_D is the diffuse transmittance of TiO_2 suspension (Fig. S4 b) of the Supplementary Information).

3.2. Radiative transfer in the photoreactor

The radiation transfer in the reactor volume can be also simplified considering the scattering "out", and assuming a 1 D model:

$$I_\lambda(z) = \langle I_{\lambda,0}\rangle_{A_R} \exp\left(-\beta_\lambda^* C_{mc} z\right) \tag{4}$$

where z is coordinate along the reactor height, and is the average incident radiation intensity at the top of the TO_2 suspension.

The average Local Volumetric Rate Photon Absorption (LVRPA) at 254 nm in the suspension volume is:

$$\langle e_\lambda^a\rangle_{V_L} = \kappa_\lambda^* C_{mc} \langle I_\lambda(z)\rangle_{V_L} \tag{5}$$

3.3. Proposed reaction mechanism and kinetic model

The proposed reaction mechanism for the CO_2 reduction and water splitting with hydrogen generation was extracted from Kočí et al. [26] and Karamian and Sharifnia [32]. In Fig. 2 simplified mechanism considering global reaction can be observed. Carbon species competes with protons to capture electrons in the conduction band. The main by-products detected in this work were hydrogen, methane and carbon monoxide. On the other hand, the reduced species (as the main products CO, CH_4 and H_2 detected in this work) can also be oxidized by the h^+ or $HO^\cdot$ generated in the valence band. Therefore, the kinetic of this photocatalytic system reaches a steady state where the reduction rate equals the oxidation rate, observing a plateau for products yields.

Based on the above mechanism and on the global steps and reaction rates summarized in Table 2, where the products are formed and then oxidezed by holes or $HO^\cdot$, the following local reaction rate for each detected by-product per unit of the photocatalytic surface is proposed, which is a potential function of the light intensity:

$$r_{CO} = (\alpha_1 - \alpha_2[CO])\langle I\rangle_{V_L}^n \tag{6}$$

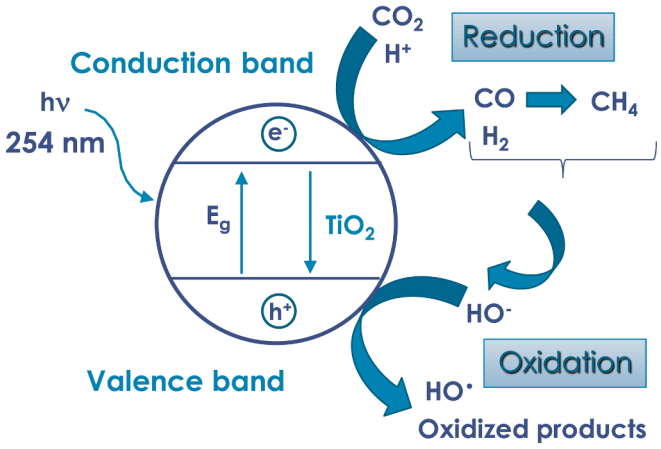

Fig. 2. Global reaction mechanism for photocatalytic CO_2 reduction and water splitting.

Table 2
Global reaction paths during photocatalytic CO_2 reduction and water splitting.

Global reaction step					Rate
CO_2	+	e^-	→	*CO*	$\alpha_1\langle I\rangle_{V_L}^n$
CO	+	$HO^\bullet/h^+$	→	Oxidized Products	$\alpha_2[CO]\langle I\rangle_{V_L}^n - \alpha_2'[CO]\langle I\rangle_{V_L}^n$
CO	+	e^-	→	CH_4	$\alpha_2'[CO]\langle I\rangle_{V_L}^n$
CH_4	+	$HO^\bullet/h^+$	→	Oxidized Products	$\alpha_3[CH_4]\langle I\rangle_{V_L}^n$
H^+	+	e^-	→	H_2	$\alpha_4\langle I\rangle_{V_L}^n$
H_2	+	$HO^\bullet/h^+$	→	Oxidized Products	$\alpha_5[H_2]\langle I\rangle_{V_L}^n$

$$r_{CH_4} = \left(\alpha_2'[CO] - \alpha_3[CH_4]\right)\langle I\rangle_{V_L}^n \tag{7}$$

$$r_{H_2} = (\alpha_4 - \alpha_5[H_2])\langle I\rangle_{V_L}^n \tag{8}$$

Where α_i are the reaction rate constants, n is the reaction order regarding the light intensity, and $\langle I\rangle_{V_L}$ is average light intensity in the liquid phase of the photoreactor. It should be noted that every reaction rate term is first order regarding the reactant concentration, with the exception of the reaction rate of protons and CO_2 reduction, since these reactants (H^+ and CO_2) are in excess and can be considered as a zero order reaction rate (the reduction rate of H^+ and CO_2 are equal to $\alpha_1\langle I\rangle_{V_L}^n$ and $\alpha_4\langle I\rangle_{V_L}^n$, respectively).

The main products detected in the gas phase during the photocatalytic reaction were CO, CH_4, and H_2. It is likely that any oxidized products mentioned in Table 2 would arise from the oxidation of these primary products by HO· or h^+ (e.g. from the oxidation of CH_4 and CO back to CO_2). Given these conditions, other potential oxidized products would be present in very low concentrations, likely below the detection limit.

3.4. Mass balance

Considering a pseudo-homogenous system and perfect mixing conditions in the liquid phase, the mass balance of each species reads:

$$\varepsilon\frac{dC_{L,i}}{dt} = \varepsilon a_V^{TiO_2}\langle r_i\rangle_{V_L} - a_V^{G-L} r_{G-L,i} \tag{9}$$

On the other hand, the mass balance of the by-products in the gas phase under perfect mixing conditions reads:

$$(1-\varepsilon)\frac{dC_{G,i}}{dt} = a_V^{G-L} r_{G-L,i} \tag{10}$$

where $C_{L,i}$ and $C_{G,i}$ are the molar concentration in the liquid and gas phases respectively, $i = CO, CH_4, H_2$ the main observed by-products, $\langle r_i\rangle_{V_L}$ is the average superficial reaction rate in the liquid phase volume, $r_{G-L,i}$ is the liquid–gas mass transfer rate, $\varepsilon = V_L/V_R$, $a_V^{TiO_2}$ is the active catalytic surface are per unit of reactor volume:

$$a_V^{TiO_2} = \frac{A^{TiO_2}}{V_R} = S_g C_{mc} \tag{11}$$

and a_V^{G-L} is the gas − liquid interfacial area per unit of reactor volume:

$$a_V^{G-L} = \frac{A^{G-L}}{V_R} = \frac{1}{H_R} \tag{12}$$

where S_g is the specific surface of the photocatalyst, C_{mc} is the photocatalyst load, A^{TiO_2} is the total area of TiO_2, and A^{G-L} is the liquid–gas interface area.

According to the thin film theory, the mass transfer flux in the G-L interface can be expressed as:

$$r_{G-L,i} = k_{G-L}\left(C_{L,i} - C_{L,i}^{int}\right) = k_{G-L}\left(C_{L,i} - HC_{G,i}\right) \tag{13}$$

where $C_{L,i}^{int}$ is the by-product concentration in the interphase, H is the Henry's law constant and k_{G-L} is the G-L mass transfer coefficient.

For gas - liquid mass transfer in a stirred vessel the following correlation for the Sherwood number can be postulated [33]:

$$Sh = \frac{k_{G-L} D_R}{D_{iB}} = aRe^b Sc^c \quad (14)$$

With $Re = \frac{ND_R^2\rho}{\mu}$ the Reynolds number, $Sc = \frac{\mu}{\rho D_{iB}}$ the Schmidt number, D_R the diameter of the stirred tank, N the angular velocity of the stirred tank, D_{iB} the diffusion coefficient of the compound i (H_2, CH_4 or CO) in B (water), ρ water density and μ viscosity of water.

So, the following expression can be postulated for the mass transfer coefficient in function of the stirring speed N:

$$k_{G-L} = k' N^b \quad (15)$$

Where k' and b are parameters to be determined with the experimental data.

4. Results and discussion

4.2. Photocatalyst characterization

From the UV–Vis diffuse reflectance spectra, the identified energy absorption edge of the synthetized photocatalyst resulted in 3.26 eV. These results are shown in Figs. S5 and S6 of the Supplementary Information.

Regarding the structural parameters of the TiO_2, 100 % anatase was identified with a crystallite size of about 14.4 nm (Table S1 and Fig. S7 of the Supplementary Information).

The spectral optical properties of measured specular transmittance (T_S), diffuse transmittance (T_D) and diffuse reflectance (R_D) are shown in Fig. S4 of the Supplementary Information.

4.2. Radiation field

From experimental specular transmittance at 254 nm (Fig. S4 a) of the Supplementary Information) and performing a linear regression of - ln T_S vs. C_{mc} L (Fig. 3), according to Eq. (1) the extinction coefficient can be obtained. Then, from the linear regression:

$$\beta^*_{\lambda=254nm} = 4.674 L \bullet g^{-1} \bullet cm^{-1}$$

In similar way, from experimental diffusive transmittance (T_D) at 254 nm (Fig. S4 b) of the Supplementary Information) and performing a linear regression of - ln T_D vs. C_{mc} L (Fig. 4), according to Eq. (2) the absorption coefficient can be obtained. Then, from the liner regression:

$$\kappa^*_{\lambda=254nm} = 3.355 L \bullet g^{-1} \bullet cm^{-1}$$

The boundary condition for the radiation transfer equation (Eq. 4) is assumed as an average of the light intensity at the radiation inlet surface. According to the radiometer measurements done on the liquid suspension-gas surface employing as illumination source the pen ray lamp (λ=254 nm) shown in Fig. S3 of the Supplementary Information, the average incident radiation flux is $\langle I_{\lambda,0}\rangle_{A_R} = 131.98\,mW \bullet cm^2$.

The light intensity distributions through the reactor height predicted by Eq. (4) for different photocatalyst mass concentrations are shown in Fig. 5. The higher the photocatalyst load in the reactor, the faster light extinction within the reaction mixture due to its high radiation absorption. At lower photocatalyst load of 0.5 g · L^{-1} the light distribution is more uniform and the dark zone is almost negligible. This phenomenon can be also observed in Fig. 6, where the calculated average light intensities in the suspension volume decreases with the photocatalyst concentration.

On the other hand, the calculated average Local Volumetric Rate Photon Absorption (LVRPA) at 254 nm in the suspension volume is shown in Table S2 of the Supplementary Information for different photocatalyst load. Similar values of the LVRPA can be observed for different TiO_2 load as the result of combination effect of light intensity distribution in the photoreactor and the photocatalyst amount. When the TiO_2 mass concentration is low, less radiation is absorbed but light intensity is better distributed in the reaction volume, then the average LVRPA does not change appreciably. Therefore, average light intensity in the reactor is a more appropriate radiation parameter to correlate the observed products yields applying different TiO_2 loads.

4.2. Kinetic parameter optimization

The estimation of the kinetic and mass transfer parameters of the proposed model in Section 3 ($Sg\alpha_i$, n, k', and b) was done with a

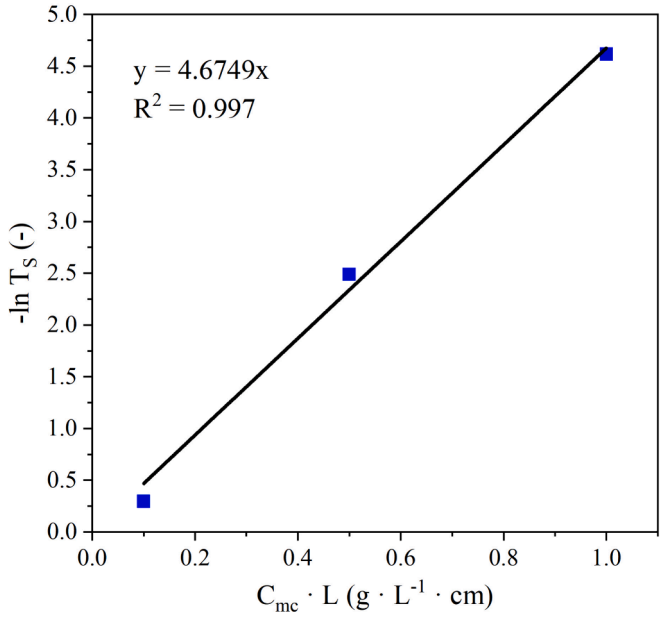

Fig. 3. Linear regression of natural logarithm of the specular transmittance (T_S) vs. catalyst load (C_{mc}) per spectrophotometer path length at 254 nm.

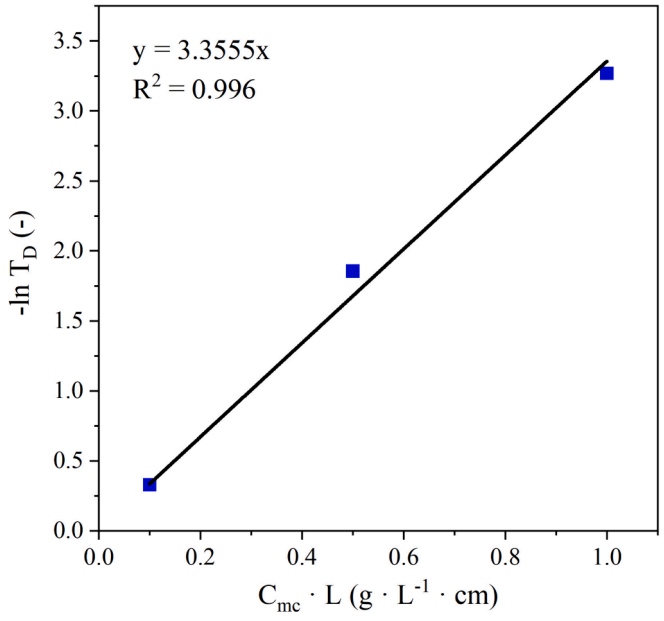

Fig. 4. Linear regression of natural logarithm of the diffuse transmittance (T_D) vs. catalyst load (C_{mc}) per spectrophotometer path length at 254 nm.

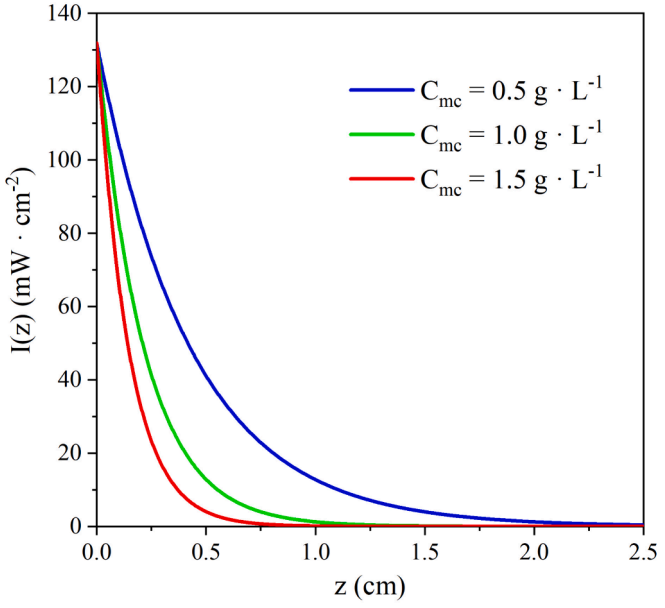

Fig. 5. Light intensity extinction at 254 nm through the reactor height for different photocatalyst load.

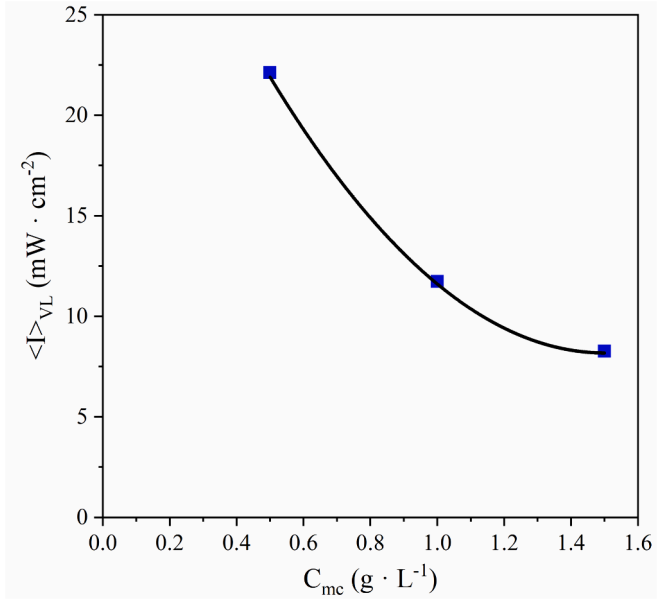

Fig. 6. Average light intensity in the suspension volume for different photocatalyst loads at 254 nm.

nonlinear regression tool that applies the Generalized Reduced Gradient algorithm. The differential equations of the species mass balances were solved applying the finite difference numerical method. The Root Mean Square Error (RMSE) calculated with the numerical solution of the mass balance in the gas phase (that is linked with the mass balance in the liquid, the reacting phase) and with the experimental results of the formed products expressed as volumetric concentration was minimized during the nonlinear regression. The total RMSE between experiments and predictions was about 20.7 % considering all performed experiments.

Table 3 summarizes the estimated values of the model parameters along with other input model parameters (as the Henry law constant for each product).

4.3. Effect of the stirring speed

In the first series of experiments change in the magnetic stirrer speed was tested. The volume of NaOH solution was 120 mL and photocatalyst amount was 0.12 g ($C_{mc} = 1\ g \cdot L^{-1}$). The stirring of the reaction mixture was 300, 500 and 700 rpm. The highest photocatalytic activity was achieved using a stirrer speed of 700 rpm. The products yields per unit of gas phase volume at the time of 8 h from the start of irradiation was 19.85 μmol · L^{-1} of H_2, 0.78 μmol · L^{-1} of CH_4 and 0.28 μmol · L^{-1} of CO.

Fig. 7 shows the experimental and model evolution of gas phase concentration of methane, carbon monoxide and hydrogen varying the stirring speed. Increasing the stirring speed, a higher yield is observed because the mass transfer rate of the by-products from liquid to gas is accelerated. According to proposed Eq. (15), when the stirring is speeded up, the mass transfer coefficient increases approximately linearly with the angular velocity ($b = 1.18$). Therefore, byproducts are transferred from liquid to gas phase quicker when the turbulence increases in the stirred tank.

However, even for the highest stirring speed tested, the products yields reach a plateau for longer reaction times. As discussed above, the proposed reaction mechanism self-limits the products formation since they can be oxidized by holes or hydroxyl radical during the photocatalytic reaction (Fig. 2).

4.4. Effect of the photocatalyst concentration

In the second series of experiments the amount of suspended photocatalyst in the stirred tank was changed. The volume of NaOH solution was 120 mL and the stirrer speed was 700 rpm. The amount of photocatalyst was 0.06 (0.5 g · L^{-1}), 0.12 (1 g · L^{-1}) and 0.18 (1.5 g · L^{-1}) grams. The highest photocatalytic activity was achieved with photocatalyst concentration of 0.5 g · L^{-1}. The products yields per unit of gas phase volume at the time of 8 h from the start of irradiation was 36.65 μmol · L^{-1} of H_2, 0.87 μmol · L^{-1} of CH_4 and 0.34 μmol · L^{-1} of CO.

Fig. 8 shows the evolution the gas phase concentration of methane, carbon monoxide and hydrogen varying the photocatalyst load experimentally measured and predicted by the model. A lower photocatalyst load results in higher conversions of CO_2 into the byproducts. This can be attributed to a more uniform radiation field in the photocatalyst

Table 3
Kinetic and mass transfer parameters.

Kinetic parameters			Mass transfer parameters		
Constant	**Value**	**Units**	**Constant**	**Value**	**Units**
$Sg\ \alpha_1$ [CO_2]	1.45×10^7	$mol \cdot g^{-1} \cdot h^{-1} \cdot dm^{2n} \cdot W^{-n}$	b	1.18	–
$Sg\ \alpha_2$	1.86×10^9	$L \cdot g^{-1} \cdot h^{-1} \cdot dm^{2n} \cdot W^{-n}$	k'_{CO}	0.04008	$dm \cdot h^{-1} \cdot rpm^{-b}$
$Sg\ \alpha'_2$	1.10×10^{10}	$L \cdot g^{-1} \cdot h^{-1} \cdot dm^{2n} \cdot W^{-n}$	k'_{CH_4}	0.02211	$dm \cdot h^{-1} \cdot rpm^{-b}$
$Sg\ \alpha_3$	2.06×10^9	$L \cdot g^{-1} \cdot h^{-1} \cdot dm^{2n} \cdot W^{-n}$	k'_{H_2}	0.03244	$dm \cdot h^{-1} \cdot rpm^{-b}$
$Sg\ \alpha_4$	4.45×10^8	$mol \cdot g^{-1} \cdot h^{-1} \cdot dm^{2n} \cdot W^{-n}$	H_{CO}	2.30×10^{-2}	–
$Sg\ \alpha_5$	5.80×10^8	$L \cdot g^{-1} \cdot h^{-1} \cdot dm^{2n} \cdot W^{-n}$	H_{CH_4}	3.20×10^{-2}	–
n	4.01		H_{H_2}	1.90×10^{-2}	–

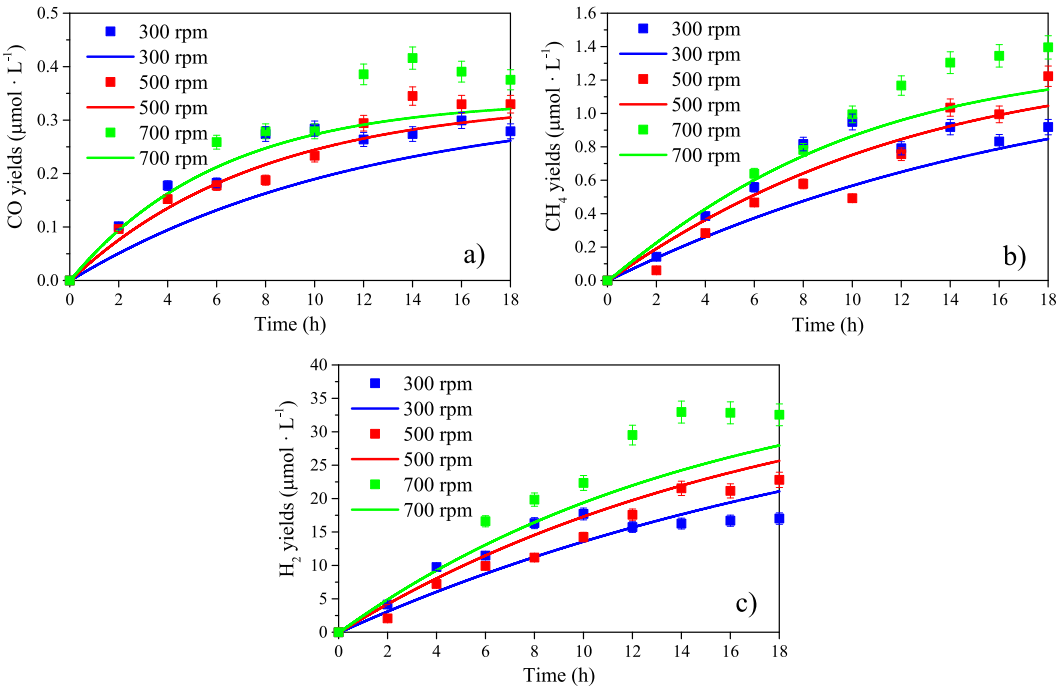

Fig. 7. Experimental results and model predictions of the gas phase concentration of a) CO, b) CH_4 and c) H_2 on varying stirring speed: points = experimental data, lines = calculated data. C_{mc} = 1 g · L^{-1}.

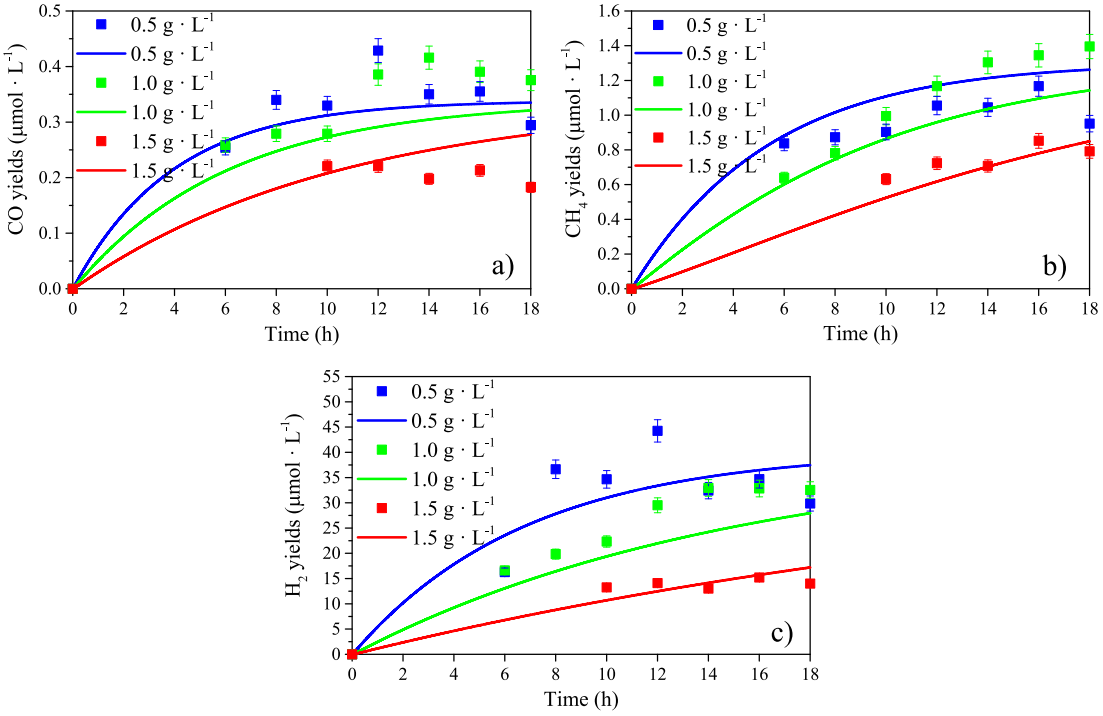

Fig. 8. Experimental results and model predictions of the gas phase concentration of a) CO, b) CH_4 and c) H_2 on varying photocatalyst load: points = experimental data, lines = calculated data. N = 700 rpm.

suspension for lower catalyst load, and therefore smaller dark zone where no photocatalytic reaction occurs. On the other hand, more active surface area can be expected since less particles agglomerations are formed for lower photocatalyst mass concentration [34].

This is in concordance with the results observed in Edelmannová et al. [35] during photocatalytic H_2 production, where the maximum hydrogen yield was found for a photocatalyst concentration of 0.25 g · L^{-1} (not tested in this work). The product yield decreased for the lowest photocatalyst concentrations (0.1 g · L^{-1}) due to less available total active area. On the other hand, for higher photocatalyst concentration, the radiation was extinguished faster and bigger particles agglomerations were more likely to be formed.

Still, the performance of this reaction and the conversion of CO_2 is very low, on one hand because the initial amount of CO_2 in gas phase is

Table 4
Comparison of experimental and calculated data for various stirring speeds and photocatalysts concentrations.

Experimental conditions C_{mc} (g · L^{-1})	N (rpm)	Product	Area under experimental curve	Area under calculated curve	Difference of calculated from experimental (%)
1	300	CO	4.00 ± 0.20	2.91	27.21
		CH_4	11.68 ± 0.58	8.81	24.57
		H_2	233.39 ± 11.67	212.31	9.03
1	500	CO	3.91 ± 0.20	3.71	5.06
		CH_4	10.63 ± 0.53	11.51	−8.31
		H_2	233.87 ± 11.69	268.48	−14.80
1	700	CO	4.88 ± 0.24	4.14	15.24
		CH_4	15.28 ± 0.76	13.09	14.36
		H_2	384.53 ± 19.23	299.52	22.11
0.5	700	CO	5.07 ± 0.25	4.78	5.72
		CH_4	14.33 ± 0.72	16.78	−17.09
		H_2	493.73 ± 24.69	470.17	4.77
1.0	700	CO	4.91 ± 0.25	4.14	15.78
		CH_4	15.28 ± 0.76	13.09	14.36
		H_2	376.35 ± 18.82	299.52	20.41
1.5	700	CO	2.97 ± 0.15	3.18	−7.04
		CH_4	9.53 ± 0.48	8.20	13.96
		H_2	187.11 ± 9.36	168.83	9.77

very high (almost 100 %), and on the other hand, because the products yields are relatively low. The CO_2 conversion in these systems can reach values of about 0.1 % [36].

To gain a more precise understanding of the correspondence between the calculated and experimental data, a comparison of area under the curve in time from 0 to 18 h was performed. The calculated data form a distinct line, allowing for a clear determination of the area under the curve. In contrast, the experimental data, characterized by a limited number of points, underwent polynomial fitting ($R^2 > 0.99$) initiated at 0. The area under the polynomial fit was integrated for each dataset (Table 4). Table 4 shows surprisingly good agreement of calculated and experimental data. Across the majority of experimental conditions, the difference between the two sets of data is less than 15 %. It is important to mention the extreme complexity of photocatalytic reduction of CO_2 with multiple concurrent reactions taking place. Therefore, the calculation method was slightly simplified and still nicely match the experimental data, showing the same tendency, within the margin of the experimental error, for the total amount of formed products when photocatalyst load and stirring speed is varied.

Given the relatively good agreement between experimental data and data derived from the model, predictions of product yields were made for another set of reaction conditions, specifically stirring speed of 900 rpm and photocatalyst concentration of 0.25 g · L^{-1}, to see whether the product yields would keep increasing with decreasing photocatalyst concentration and increasing stirring speed. The effect of higher stirring speed (900 rpm) with photocatalyst concentration of 1 g · L^{-1} is depicted in Fig. 9.

Analysis of the calculated data reveals that elevating the stirring speed from 300 to 500 rpm results in a respective 16 %, 23 %, and 21 % increase in CO, CH_4, and H_2 products. While the yields of all products continue to rise with further increase of stirring speed, the growth becomes less pronounced. Comparing product yields at 700 rpm (calculated data) to those at 900 rpm (calculated data), it becomes evident that the incremental increase is modest at best: 2 %, 5 %, and 5 % for CO, CH_4, and H_2, respectively. From a certain value of stirrer speed, the products mass transfer from liquid to gas phase would be high enough

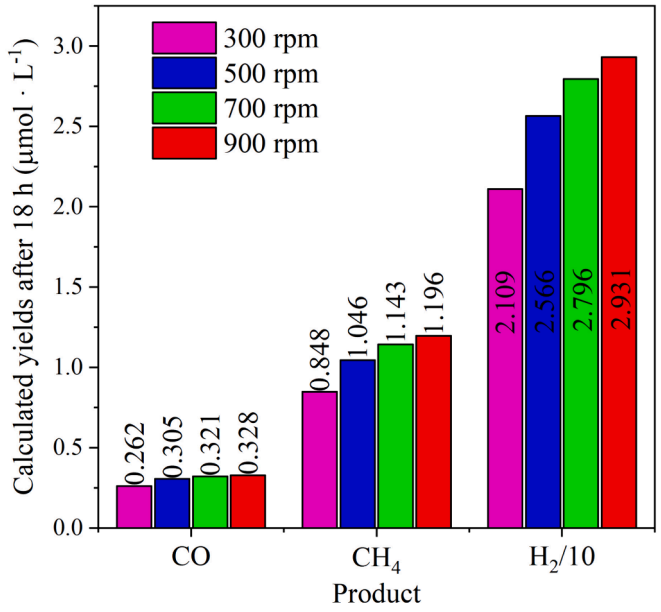

Fig. 9. Calculated data predictions of the gas phase concentration of products after 18 h of irradiation on varying stirring speed. C_{mc} = 1 g · L^{-1}.

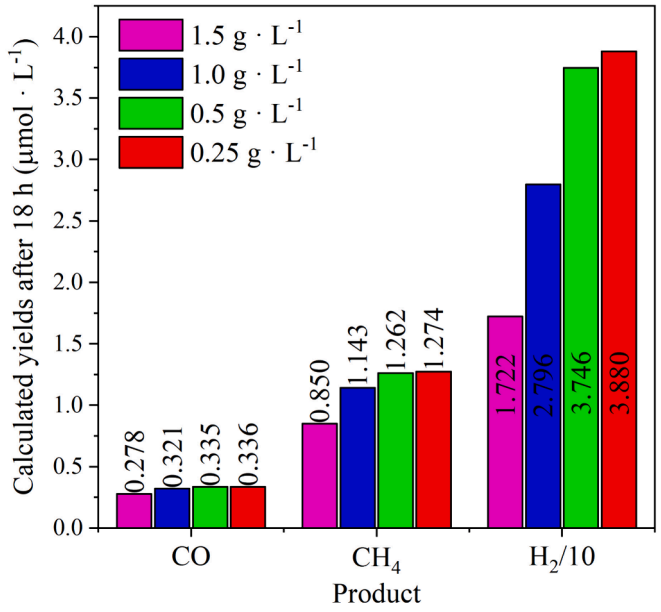

Fig. 10. Calculated data predictions of the gas phase concentration of products after 18 h of irradiation on varying photocatalyst concentration. N = 700 rpm.

for not to be the limiting step of the reaction and the products yields in gas phase would state constant.

Similarly, predictions of product yields were made for a reduced photocatalyst concentration at 700 rpm (Fig. 10). The impact of catalyst concentration proves to be significantly more pronounced than the effect of stirring speed, and this observation correlates with radiation intensity (Figs. 5 and S8). Especially in case of photocatalyst concentration 0.25 $g \cdot L^{-1}$ the light reaches much further into the suspension and the average light intensity in the suspension volume is higher (see Fig. S9 of the Supplementary Information).

Upon decreasing the catalyst concentration from 1.5 $g \cdot L^{-1}$ to 1 $g \cdot L^{-1}$, the product yields of CO, CH_4, and H_2 exhibited respective increase of 15 %, 34 %, and 62 %. Further reduction in catalyst concentration (to 0.5 $g \cdot L^{-1}$) once again led to increased product yields, although not as dramatically. A comparison of product yields at a concentration of 0.5 $g \cdot L^{-1}$ and 0.25 $g \cdot L^{-1}$ (calculated data) reveals a marginal increase: 0 %, 1 %, and 4 % for CO, CH_4, and H_2, respectively.

Based on the findings, predictions of yields were extrapolated at an optimal speed of 900 rpm and a photocatalyst concentration of 0.25 $g \cdot L^{-1}$. According to the model, the anticipated product yields for CO, CH_4, and H_2 would be 0.34, 1.29, and 39.82 $\mu mol \cdot L^{-1}$, respectively. The significance of these calculations underscores the imperative need for dedicated experiments tailored for each photocatalyst type. These experiments should precisely delineate the optimal reaction conditions, with particular emphasis on the pivotal factor of catalyst concentration. This factor plays a critical role in photocatalytic reactions, interlinked with the extinction of light intensity.

5. Conclusions

The effect of the main operating conditions of photocatalyst concentration and stirring speed on the photocatalytic reduction of CO_2 in a slurry batch photoreactor was studied employing a synthetized TiO_2. A simplified photocatalytic kinetic model including the radiation field in the photoreactor was proposed and the mass transfer from liquid to gas phase of the main detected reaction by-products, CO, CH_4 and H_2, was considered. A very good agreement between the experimental data and mathematical model predictions was observed. The proposed models can explain the effect of different operating conditions on the CO, CH_4 and H_2 yields: i) The magnetic stirrer speed influences the gas – liquid mass transfer rate. Faster stirring speed of the liquid phase guarantees quicker species transport to the gas phase. However, further increase to 900 rpm has only marginal effect. ii) The TiO_2 photocatalyst mass concentration affects the available total active surface and the irradiation absorbance in the photoreactor volume. The best product yields were observed for the lowest tested photocatalyst concentration (0.5 $g \cdot L^{-1}$), which presents better irradiation distribution in the reaction media and less particles agglomeration providing higher available active surface for the reaction. The calculation model was used to predict the product yields in the presence of even lower photocatalyst concentration of 0.25 $g \cdot L^{-1}$. The increase of predicted yields was marginal in this case as well. The obtained kinetics in this work is valuable information for the CO_2 photocatalytic reduction scaling up and optimization.

CRediT authorship contribution statement

María de los Milagros Ballari: Writing – original draft, Visualization, Software, Methodology, Investigation, Formal analysis, Conceptualization. **Miroslava Filip Edelmannová:** Writing – review & editing, Validation, Methodology, Investigation, Formal analysis, Data curation. **Rudolf Ricka:** Writing – review & editing, Investigation, Formal analysis. **Martin Reli:** Writing – review & editing, Writing – original draft, Software, Methodology, Investigation, Formal analysis, Conceptualization. **Kamila Kočí:** Writing – review & editing, Supervision, Resources, Project administration, Conceptualization.

Declaration of competing interest

The authors declare that they have no known competing financial interests or personal relationships that could have appeared to influence the work reported in this paper.

Data availability

Data will be made available on request.

Acknowledgements

The work was supported by Large Research Infrastructure ENREGAT (project No. LM2023056), and GA CR project 21-24268 K. MMB is grateful to Universidad Nacional del Litoral (UNL, CAI + D 50620190100162LI), Consejo Nacional de Investigaciones Científicas y Técnicas (CONICET, PIP-2015 0100093) and Agencia Nacional de Promoción Científica y Tecnológica (ANPCyT, PICT 2017-2090) from Argentina for the financial support.

Appendix A. Supplementary data

Supplementary data to this article can be found online at https://doi.org/10.1016/j.ecmx.2024.100651.

References

[1] International Energy Agency (IEA), Global Energy Review 2021. 2021.
[2] Liu L, Li Y. Understanding the reaction mechanism of photocatalytic reduction of CO_2 with H_2O on TiO_2-based photocatalysts: A Review. Aerosol Air Qual Res 2014;14:453–69.
[3] Xiong H, Dong Y, Liu D, Long R, Kong T, Xiong Y. Recent advances in porous materials for photocatalytic CO_2 reduction. J Phys Chem Lett 2022;13:1272–82.
[4] Domínguez-Espíndola RB, Arias DM, Rodríguez-González C, Sebastian PJ. A critical review on advances in TiO_2-based photocatalytic systems for CO_2 reduction. Appl Therm Eng 2022;216:119009.
[5] Maarisetty D, Mary R, Hang DR, Mohapatra P, Sundar BS. The role of material defects in the photocatalytic CO_2 reduction: Interfacial properties, thermodynamics, kinetics and mechanism. Journal of CO_2 Utilization 2022;64:102175.
[6] Fan WK, Tahir M. Recent advances on cobalt metal organic frameworks (MOFs) for photocatalytic CO_2 reduction to renewable energy and fuels: A review on current progress and future directions. Energ Conver Manage 2022;253:115180.
[7] Mohtaram S, Mohtaram MS, Sabbaghi S, You X, Wu W, Golsanami N. Enhancement strategies in CO_2 conversion and management of biochar supported photocatalyst for effective generation of renewable and sustainable solar energy. Energ Conver Manage 2024;300:117987.
[8] Pan H, Li Y, Zhu L, Lu Y. Solar-driven H_2O/CO_2 conversion to fuels via two-step electro-thermochemical cycle in a solid oxide electrochemical cell. Energ Conver Manage 2022;259:115578.
[9] Fu L, Ren Z, Si W, Ma Q, Huang W, Liao K, et al. Research progress on CO_2 capture and utilization technology. Journal of CO_2 Utilization 2022;66:102260.
[10] Hong WY. A techno-economic review on carbon capture, utilisation and storage systems for achieving a net-zero CO_2 emissions future. Carbon Capt Sci Technol 2022;3:100044.
[11] Roncancio R, Gore JP. CO_2 char gasification: A systematic review from 2014 to 2020. Energy Convers Manage: X 2021;10:100060.
[12] Banu A, Mir N, Ewis D, El-Naas MH, Amhamed AI, Bicer Y. Formic acid production through electrochemical reduction of CO_2: A life cycle assessment. Energy Convers Manage: X 2023;20:100441.
[13] Zhang L, Zhao Q, Shen L, Li Q, Liu T, Hou L, et al. Enhancing the photocatalytic activity of defective titania for carbon dioxide photoreduction via surface functionalization. Cat Sci Technol 2022;2:509–18.
[14] Sun Z, Talreja N, Tao H, Texter J, Muhler M, Strunk J, et al. Catalysis of carbon dioxide photoreduction on nanosheets: fundamentals and challenges. Angew Chem Int Ed 2018;26:7613–27.
[15] Reli M, Nadrah P, Filip EM, Ricka R, Sever ŠA, Lavrenčič ŠU, et al. Photocatalytic CO_2 reduction over mesoporous TiO_2 photocatalysts. Mater Sci Semicond Process 2024;169:107927.
[16] Habisreutinger SN, Schmidt-Mende L, Stolarczyk JK. Photocatalytic reduction of CO_2 on TiO_2 and other semiconductors. Angew Chem Int Ed 2013;52:7372–408.
[17] Pham K, Ali-Löytty H, Saari J, Zubair M, Valden M, Lahtonen K, et al. Functionalization of TiO_2 inverse opal structure with atomic layer deposition grown Cu for photocatalytic and antibacterial applications. Opt Mater 2022;131:112695.
[18] Filip EM, Reli M, Nadrah P, Rozman N, Ricka R, Sever ŠA, et al. A comparative study of TiO_2 preparation method on their photocatalytic activity for CO_2 reduction. Catal Today 2023;413–415:113944.

[19] Sun Y, Ji H, Sun Y, Zhang G, Zhou H, Cao S, et al. Synergistic Effect of Oxygen Vacancy and High Porosity of Nano MIL-125(Ti) for Enhanced Photocatalytic Nitrogen Fixation. Angew Chem Int Ed 2024;63:e202316973.
[20] Hafeez HY, Lakhera SK, Narayanan N, Harish S, Hayakawa Y, Lee B-K, et al. Environmentally Sustainable Synthesis of a $CoFe_2O_4$−TiO_2/rGO Ternary Photocatalyst: A Highly Efficient and Stable Photocatalyst for High Production of Hydrogen (Solar Fuel). ACS Omega 2019;4:880–91.
[21] Lyu W, Liu Y, Zhou J, Chen D, Zhao X, Fang R, et al. Modulating the Reaction Configuration by Breaking the Structural Symmetry of Active Sites for Efficient Photocatalytic Reduction of Low-concentration CO_2. Angew Chem Int Ed 2023;62:e202310733.
[22] Qian G, Lyu W, Zhao X, Zhou J, Fang R, Wang F, et al. Efficient Photoreduction of Diluted CO_2 to Tunable Syngas by Ni−Co Dual Sites through d-band Center Manipulation. Angew Chem Int Ed 2022;61:e202210576.
[23] Wang F, Hou T, Zhao X, Yao W, Fang R, Shen K, et al. Ordered Macroporous Carbonous Frameworks Implanted with CdS Quantum Dots for Efficient Photocatalytic CO_2 Reduction. Adv Mater 2021;33:2102690.
[24] Variar AG, Ramyashree MS, Ail VU, Shanmuga Priya SS, Sudhakar K, Tahir M. Influence of various operational parameters in enhancing photocatalytic reduction efficiency of carbon dioxide in a photoreactor: A review. J Ind Eng Chem 2021;99:19–47.
[25] Kiesgen de Richter R, Ming T, Caillol S. Fighting global warming by photocatalytic reduction of CO_2 using giant photocatalytic reactors. Renew Sustain Energy Rev 2013;19:82–106.
[26] Kočí K, Obalová L, Šolcová O. Kinetic study of photocatalytic reduction of CO_2 over TiO_2. Chem Process Eng 2010;31:395–407.
[27] Tan SS, Zou L, Hu E. Kinetic modelling for photosynthesis of hydrogen and methane through catalytic reduction of carbon dioxide with water vapour. Catal Today 2008;131:125–9.
[28] Thompson WA, Sanchez-Fernandez E, Maroto-Valer MM. Probability Langmuir-Hinshelwood based CO_2 photoreduction kinetic models. Chem Eng J 2020;384:123356.
[29] Bafaqeer A, Tahir M, Amin Nor Ashah S, Mohamed AR, Yunus Mohd Azizi C. Fabricating 2D/2D/2D heterojunction of graphene oxide mediated g-C_3N_4 and ZnV_2O_6 composite with kinetic modelling for photocatalytic CO_2 reduction to fuels under UV and visible light, Journal of Material. Science 2021;56:9985–10007.
[30] Matějová L, Polách L, Lang J, Šihor M, Reli M, Brunátová T, et al. Novel TiO_2 prepared from titanyl sulphate by using pressurized water processing and its photocatalytic activity evaluation. Mater Res Bull 2017;95:30–46.
[31] Satuf ML, Brandi RJ, Cassano AE, Alfano OM. Experimental method to evaluate the optical properties of aqueous titanium dioxide suspensions. Ind Eng Chem Res 2005;44:6643–9.
[32] Karamian E, Sharifnia S. On the general mechanism of photocatalytic reduction of CO_2. Journal of CO_2 Utilization 2016;16:194–203.
[33] Perry R. H., Green D. W., Perry's Chemical Engineering Handbook, 7th edition, 1999.
[34] Liu T-X, Liu Y, Zhang Z-J, Li F-B, Li X-Z. Comparison of aqueous photoreactions with TiO_2 in its hydrosol solution and powdery suspension for light utilization. Ind Eng Chem Res 2011;50:7841–8.
[35] Edelmannová M, Ballari MM, Pribylc M, Kocí K. Experimental and modelling studies on the photocatalytic generation of hydrogen during water-splitting over a commercial TiO_2 photocatalyst P25. Energ Conver Manage 2021;245:114582.
[36] Kočí K, Obalová L, Matějová L, Plachá D, Lacný Z, Jirkovský J, et al. Effect of TiO_2 particle size on the photocatalytic reduction of CO_2. Appl Catal B 2009;89(3–4):494–502.